Ru^{II} photosensitizer functionalized two-dimensional MoS_2 for light-driven hydrogen evolution

Xin Chen,[a,b] David McAteer,[a,c] Cormac McGuinness,[a,c] Ian Godwin,[a,c] Jonathan N. Coleman,[a,c] Aidan R. McDonald*[a,b]

Abstract: *Metallic-phase molybdenum disulfide (1T-MoS_2) nanosheets have proven to be highly active in the hydrogen evolution reaction (HER). We describe construction of photosensitizer functionalized 1T-MoS_2 by covalently tethering the molecular photosensitizer $[Ru^{II}(bpy)_3]^{2+}$ (bpy = 2,2'-bipyridine) on 1T-MoS_2 nanosheets. This was achieved by covalently tethering the bpy ligand to 1T-MoS_2 nanosheets, and subsequent complexation with $[Ru^{II}(bpy)_2Cl_2]$ to yield $[Ru^{II}(bpy)_3]$-MoS_2. The obtained $[Ru^{II}(bpy)_3]$-MoS_2 nanosheets were characterized using Infra-red, electronic absorption, X-ray photoelectron, and Raman spectroscopies, X-ray powder diffraction and electron microscopy. The fabricated material exhibited a significant improvement of photocurrent and HER performance, demonstrating the potential of such two-dimensional $[Ru^{II}(bpy)_3]$-MoS_2 constructs in photosensitized HER.*

Hydrogen (H_2) is regarded as an ideal alternative fuel source due to its high energy density and environmentally friendly combustion process.[1-6] H_2 production is currently mainly reliant on steam reforming of natural gases such as methane.[7-8] However, this process involves a large amount of fossil fuel consumption and greenhouse gas emission, therefore it is not a sustainable or carbon-neutral process. Solar-driven water splitting can be accomplished by a photoelectrochemical (PEC) system.[1, 9-10] The typical PEC system consists of two components: light absorber and an electrocatalyst which catalyzes the hydrogen evolution reaction (HER). HER is often mediated by Pt, which displays negligible over potential and excellent kinetics.[11] However, Pt's scarcity and high cost makes it commercially unfeasible.

Recently, exfoliated transition-metal dichalcogenides (TMDs), in particular two-dimensional (2D) MoS_2, have evoked considerable interest in electrocatalytic HER, due to their excellent catalytic activities, and act as an abundant alternative to Pt.[12-13] MoS_2 mainly exists in two phases (2H or 1T): in the 2H-phase, the coordination of Mo is trigonal prismatic; while in the 1T-phase, the Mo atom has an octahedral coordination environment. Monolayer 2H-MoS_2 is a semiconductor with a 1.9 eV bandgap, while 1T-MoS_2 displays a metallic nature.[14] Early attempts to employ MoS_2 for catalyzing the HER have shown that bulk MoS_2 was not an active HER catalyst due to the limited active sites and unfavorable conductivity,[15] whereas nanostructured MoS_2 showed significantly improved HER activity.[16] Both theoretical and experimental investigations revealed that the edges of MoS_2 were catalytically active while the basal plane remained inert.[17] Chhowalla later demonstrated that phase transition from 2H- to 1T-MoS_2 via lithium intercalation can enhance the HER activity, which could be attributed to an active basal plane.[18-19]

Electrochemical HER by MoS_2 has been studied in detail,[16, 20-21] however, photoelectrochemical HER by MoS_2 remains in its infancy. The use of monolayer 2H-MoS_2 as a photocathode (2H-MoS_2 acts as both light absorber and electrocatalyst) for H_2 generation has displayed poor performance.[22-23] One strategy to circumvent this is to combine photo-absorbers with MoS_2. Recent studies have shown that MoS_2 has been combined with semiconductor-based light absorbers such as Si, organic, and inorganic dyes for photoelectrochemical HER.[24-34] However, all of these systems lacked a linkage/tether between the dye and the MoS_2 HER catalyst, and were simply formed by mixing/physisorption, thus limiting the electronic communications between dye and catalyst, and thus inhibiting the light-driven HER efficiency. We and others have reported a variety of approaches towards tethering small molecules to TMD nanosheets.[14, 35-38] With this in mind, a covalently tethered dye sensitized 1T-MoS_2 system would hold great promise for solar driven HER. Herein, we demonstrate an approach to covalently binding the molecular photosensitizer $[Ru^{II}(bpy)_3]^{2+}$ (bpy = 2,2'-bipyridine)[39] onto 1T-MoS_2 nanosheets, and demonstrate light-driven HER from 1T-MoS_2.

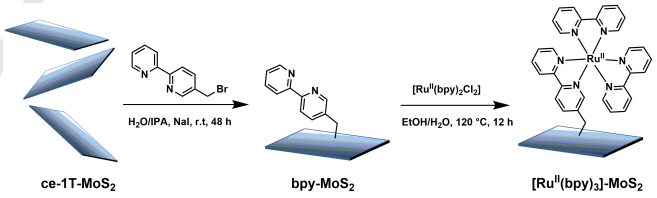

Figure 1. Schematic representation of step-wise functionalization of ce-1T-MoS_2 with $[Ru^{II}(bpy)_3]^{2+}$.

Thin layered chemically exfoliated 1T-MoS_2 (ce-1T-MoS_2) nanosheets were prepared according to a literature procedure (see supporting information for details),[14] and characterized by electronic absorption, X-ray photoelectron (XPS) and Raman spectroscopies (Figures S1-S2, S7), confirming that the exfoliated MoS_2 was predominantly the 1T-polymorph.

A step-wise functionalization of ce-1T-MoS_2 was performed (Figure 1, for details see supporting information). 5-Bromomethyl-2,2'-bipyridine was reacted with ce-1T-MoS_2 in a manner analogous to the previously reported covalent functionalization of ce-1T-MoS_2 by organoiodides.[14] 5-bromomethyl-2,2'-bipyridine (10 equiv. per ce-1T-MoS_2), pre-dissolved in propan-2-ol (IPA), 10 mL, 100-125 mM), with trace amounts of NaI (2 mg) were added to an aqueous dispersion of ce-1T-MoS_2 (20 mL, 5-6.25 mM). The mixture was sonicated in

[a] X. Chen, D. McAteer, Dr. C. McGuiness, Dr. I. Godwin, Prof. Dr. J. N. Coleman, Prof. Dr. A. R. McDonald
CRANN/AMBER Nanoscience Institute, Trinity College Dublin, The University of Dublin, College Green, Dublin 2 (Ireland)
E-mail: aidan.mcdonald@tcd.ie
[b] School of Chemistry
[c] School of Physics

Supporting information for this article is given via a link at the end of the document.

the darkness for 1 h and then subjected to magnetic stirring at room temperature for 48 hrs. The resulting dispersion was subjected to high-speed centrifugation to precipitate all the dispersed materials. The resulting product (defined as bpy-MoS_2) was washed and then re-dispersed in IPA (10 mL) for further characterization.

bpy-MoS_2 (10 mg) and $[Ru^{II}(bpy)_2Cl_2]$ (5 mg, 0.01 mmol) were combined in a water/ethanol mixture (30 mL, 1:1 v/v) and the reaction mixture was refluxed at 120 °C for 12 h. In the course of the reaction, the color changed from black to red, indicating the successful formation of a $[Ru^{II}(bpy)_3]^{2+}$-like species. The resulting functionalized material (defined as $[Ru^{II}(bpy)_3]$-MoS_2) was then separated from the reaction mixture through high-speed centrifugation, and subsequently thoroughly washed and re-dispersed in de-ionized water (5 mL) for further characterization. For comparison, bis-(2,2'-bipyridine)-(5-methyl-2,2'-bipyridine)ruthenium bis(hexafluorophosphate) ($[Ru^{II}(bpy)_2$-5-Me-bpy$)](PF_6)_2$) was also synthesized (see supporting information).

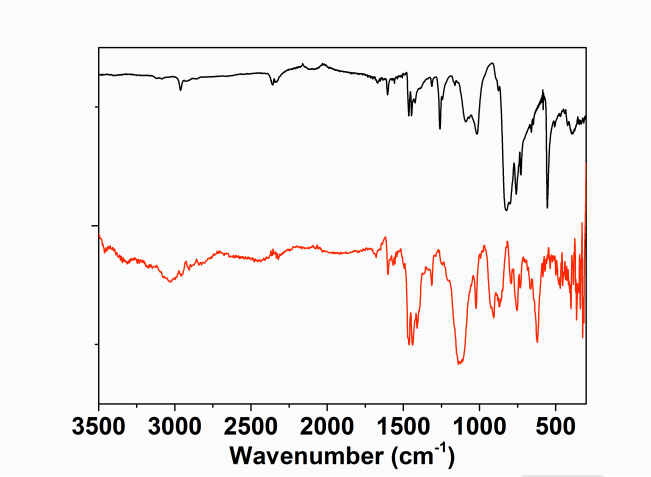

Figure 2. DRIFT spectra of $[Ru^{II}(bpy)_3]$-MoS_2 (red) and $[Ru^{II}(bpy)_2$(5-Me-bpy$)](PF_6)_2$ (black). The resonance at 823 cm^{-1} in $[Ru^{II}(bpy)_2$(5-Me-bpy$)](PF_6)_2$ attributed to PF_6^- counter ions.

Comparison of the diffuse reflectance infrared Fourier transform (DRIFT) spectra of ce-1T-MoS_2, bpy-MoS_2, $[Ru^{II}(bpy)_3]$-MoS_2, and $[Ru^{II}(bpy)_2$(5-Me-bpy$)](PF_6)_2$ provided proof of the tethering of $[Ru^{II}(bpy)_3]^{2+}$ to the ce-1T-MoS_2 (Figure 2 and S3). The DRIFT spectrum of bpy-MoS_2 displayed features in the range of 1302 to 1630 cm^{-1} associated with $\nu_{C=C}$ and $\nu_{C=N}$ modes of the bipyridine ligand. These features were shifted to higher frequencies in $[Ru^{II}(bpy)_3]$-MoS_2, suggesting the bipyridine ligand had interacted with a Ru^{II} ion (Figure S3). Critically, $[Ru^{II}(bpy)_3]$-MoS_2 exhibited nearly identical vibrational features to that of $[Ru^{II}(bpy)_2$(5-Me-bpy$)](PF_6)_2$ (Figure 2), verifying the incorporation of $[Ru^{II}(bpy)_3]^{2+}$ onto ce-1T-MoS_2. In addition, a resonance at ν = 695 cm^{-1} was detected in bpy-MoS_2. This was associated with ν_{C-S} vibrational mode, as observed previously for covalently functionalized ce-1T-MoS_2,[14, 38] confirming the formation of covalent C–S bonds upon functionalization. This peak was still discernable in $[Ru^{II}(bpy)_3]$-MoS_2, implying that the covalent linkages remained intact after complexation to the Ru^{II} ion. These observations confirm that $[Ru^{II}(bpy)_3]^{2+}$ was covalently assembled on the surface of ce-1T-MoS_2.

$[Ru^{II}(bpy)_3]$-MoS_2 displayed a markedly different electronic extinction spectrum compared to non-functionalized ce-1T-MoS_2 (Figure 3). The spectrum showed two features in the visible region: one sharp feature at λ_{max} = 304 nm and a broad shoulder centered at λ_{max} = 450 nm. In contrast, the ce-1T-MoS_2 precursor displayed two characteristic features at λ_{max} = 258 and 309 nm and no shoulder in the visible region.[40] The emergence of new features in $[Ru^{II}(bpy)_3]$-MoS_2 can be attributed to the introduced $[Ru^{II}(bpy)_3]^{2+}$ functionalities. Importantly, comparison of the electronic absorption spectra of $[Ru^{II}(bpy)_3]$-MoS_2 and $[Ru^{II}(bpy)_2$(5-Me-bpy$)](PF_6)_2$ (Figure 3) revealed that those new features in $[Ru^{II}(bpy)_3]$-MoS_2 were well matched to the ligand π to π^* band (λ_{max} = 288 nm) and metal-to-ligand charge transfer band (λ_{max} = 451 nm) of $[Ru^{II}(bpy)_2$(5-Me-bpy$)](PF_6)_2$.[41-42] Moreover, an absorbance band at λ_{max} = 550 nm, typical of the $[Ru^{II}(bpy)_2Cl_2]$ precursor, was not detected (Figure S4). This shows that there was no unreacted $[Ru^{II}(bpy)_2Cl_2]$ present.

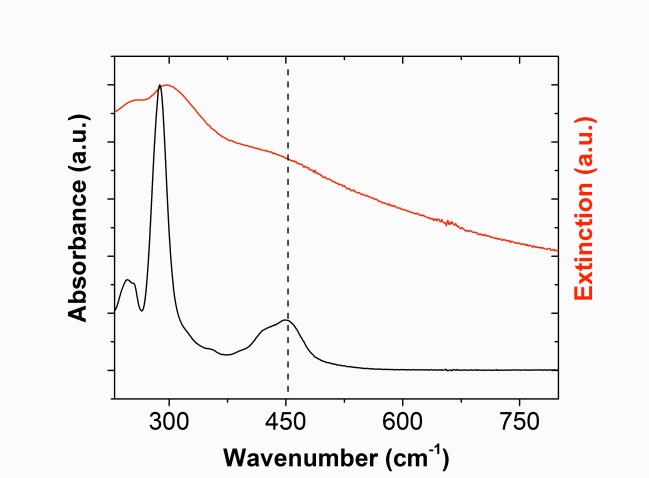

Figure 3. Electronic extinction spectrum of $[Ru^{II}(bpy)_3]$-MoS_2 (red) and absorbance spectrum of $[Ru^{II}(bpy)_2$(5-Me-bpy$)](PF_6)_2$ (black).

Atomic level inspection of both bpy-MoS_2 and $[Ru^{II}(bpy)_3]$-MoS_2 by high resolution X-ray photoelectron spectroscopy (XPS) further confirmed the chemical composition and elemental properties of the functionalized nanosheets. Compared to the precursor ce-1T-MoS_2, the XPS survey spectrum of bpy-MoS_2 (Figure S5) showed additional C (285 eV) and N (399.5 eV) elements associated with the attached bipyridine moieties, whereas no Br or I signal was detected, suggesting that coupling of 5-bromomethyl-2,2'-bipyridine to ce-1T-MoS_2 was achieved. Furthermore, the survey spectrum of $[Ru^{II}(bpy)_3]$-MoS_2 displayed additional C, N, and Ru elements deriving from the attached $[Ru^{II}(bpy)_3]^{2+}$ (Figure S6).

To gain a deeper insight into the chemical identity of the functionalities in bpy-MoS_2 and $[Ru^{II}(bpy)_3]$-MoS_2, high resolution Mo 3p/N 1s XPS spectra were recorded (Figure 4). The N 1s core level spectrum of bpy-MoS_2 was fitted with one predominant component centered at 398.7 eV, corresponding to

the N-atoms of bpy.[40] The N 1s spectrum of $[Ru^{II}(bpy)_3]$-MoS_2 displayed two distinct and intense N features at 398.3 eV and 399.8 eV, implying the presence of two types of nitrogen species. The 399.8 eV component was assigned to N-atoms that are coordinated to a Ru^{II} center; while the lower binding energy N component was assigned to uncoordinated N-atoms, as are present in bpy-MoS_2.[43] The emergence of the 399.8 eV in the post-complexation product validates our synthetic efforts of constructing the $[Ru^{II}(bpy)_3]^{2+}$ entity on the ce-1T-MoS_2 surface.[44] The loading of $[Ru^{II}(bpy)_3]^{2+}$ photosensitizer in $[Ru^{II}(bpy)_3]$-MoS_2 was estimated to be approximately 10 atomic % per MoS_2 by calculating the ratio of the amount of coordinated N- atoms to Mo-atoms according to the fitted N 1s/Mo 3p spectra (Figure 4, S7). The values of ~10% is also in the range expected from TGA analysis (Figure S8).

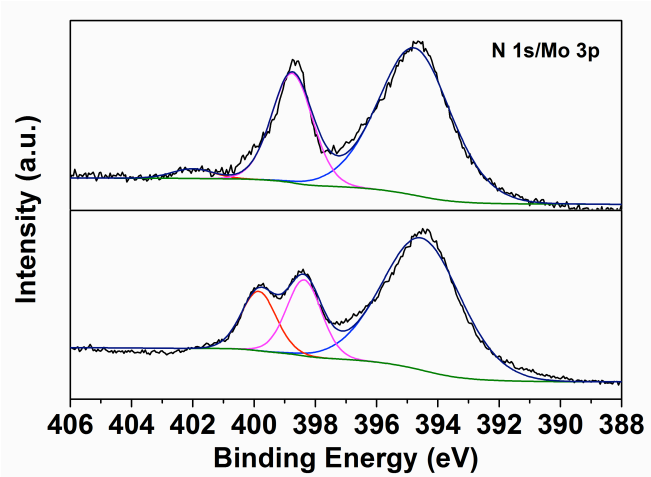

Figure 4. Fitted N 1s/Mo 3p spectra of bpy-MoS_2 (top) and $[Ru^{II}(bpy)_3]$-MoS_2 (bottom). The very weak feature at 402.0 eV assigned to quaternized N-atoms.[42]

The high-resolution S 2p core level spectrum of ce-1T-MoS_2 displayed a well-defined double-peak feature typical of ce-1T-MoS_2 (Figure S9).[38] The higher binding energy (163.5±0.2 eV) feature got more pronounced in bpy-MoS_2, indicating an increased content of electron-poor S species, which presumably derived from functionalized S-atoms (covalent C–S bond).[38, 46] Similar observations were reported for covalent functionalization of ce-1T-MoS_2 with organoiodide and diazonium salts.[14] Importantly, this feature was preserved in $[Ru^{II}(bpy)_3]$-MoS_2, indicating that the covalent linkers remain intact after complexation treatment. The fitted Mo 3d core level spectra (Figure S10) of bpy-MoS_2 and $[Ru^{II}(bpy)_3]$-MoS_2 displayed similar features to ce-1T-MoS_2 with little change upon functionalization.[14, 18] Furthermore, de-convoluted Mo 3d core level spectra (Figure S10) revealed that the proportion of 1T-phase remained predominant in both functionalized samples. This is important, because for efficient HER reactivity we require the MoS_2 to maintain the 1T phase.[18, 31]

The X-ray Powder diffraction (XRD) pattern (Figure S11) of bpy-MoS_2 showed a diffraction peak at 2Θ = 14 °, corresponding to the (002) plane of restacked MoS_2. In addition two new diffraction peaks at 2Θ = 5.6° and 10.6° were also detected, corresponding to the inter-layer expansion of 9.5 Å and 2.3 Å, which was presumably due to the attachment of bpy entities on the surface of ce-1T-MoS_2. The morphology of ce-1T-MoS_2 and $[Ru^{II}(bpy)_3]$-MoS_2 were determined by scanning electron microscopy (SEM). The SEM images displayed both materials as nanoflakes with irregular shapes and diverse lateral sizes (Figure S12). Compared to ce-1T-MoS_2, which exhibited the nanoflower-like morphology with well-defined edges, indicating the high crystallinity of the sample, $[Ru^{II}(bpy)_3]$-MoS_2 exhibited aggregations, which could be attributed to surface property changes upon functionalization. The energy dispersive X-ray (EDX) mapping (Figure S13) of $[Ru^{II}(bpy)_3]$-MoS_2 demonstrated the uniformly distributed Mo and S elements as well as Ru and N, further verifying the chemical composition of the $[Ru^{II}(bpy)_3]$-MoS_2 functionalized product.

The zeta potential of an aqueous dispersion of ce-1T-MoS_2 was determined to be -46 mV, whereas the zeta potentials of bpy-MoS_2 and $[Ru^{II}(bpy)_3]$-MoS_2 were -11 mV and 5.4 mV, respectively (Figure S14). The significantly shifted zeta potential of the functionalized samples indicated the dramatic surface changes through functionalization.[14] The Raman spectra (λ_{exc} = 632 nm, Figure S15) of ce-1T-MoS_2, bpy-MoS_2 and $[Ru^{II}(bpy)_3]$-MoS_2 demonstrated signals typical of MoS_2. Two intense peaks at ~380 cm^{-1} and ~410 cm^{-1} corresponding to in-plane E^1_{2g} and out-of-plane A_{1g} modes were observed, as well as a resonantly enhanced peak at ~450 cm^{-1} related to the 2LA(M) mode. Characteristic peaks related to 1T-MoS_2 in the range of 150-300 cm^{-1} were also identified.[47-48] Importantly, the 2LA(M) and A_{1g} modes, which are both highly sensitive to the surface chemical environment change, demonstrated considerable intensity change in the functionalized samples compared to ce-1T-MoS_2, indicating functionalization had occurred.

The PEC performance of the $[Ru^{II}(bpy)_3]$-MoS_2 was evaluated in a three-electrode electrochemical cell with 10 mM ascorbic acid electrolyte (Figure S16). The photoelectrochemical measurement was carried out using a standard three- electrode cell with a platinum (Pt) wire as the counter electrode, a saturated KCl Ag/AgCl as the reference electrode, and an indium-tin oxide (ITO) glass with samples as the working electrode in one compartment. The working electrode was prepared by drop-casting the material in aqueous dispersion onto ITO glass and dried at room temperature overnight. The mass per area for all the samples was 0.25 mg/cm^2. An ascorbic acid aqueous solution (10 mM, pH 3), prepared by dissolving of 352.2 mg of L-ascorbic acid in 200 mL of deionized water (18 MΩ cm), was used as the electrolyte and sacrificial donor. The working electrode was illuminated with a 150 W Xe lamp. The photocurrent onset potential (defined here as the potential required to reach -200 $\mu A/cm^2$) of the $[Ru^{II}(bpy)_3]$-MoS_2 photocathode was -0.35 V vs. the reversible hydrogen electrode (RHE). For comparison, the same $[Ru^{II}(bpy)_3]$-MoS_2 electrode was also tested with no illumination, exhibiting the maximum current of -170 $\mu A/cm^2$ at -0.35 V vs. RHE. The photocathode was also tested over an extended time period (24 h) displaying no depletion in current density in the period (Figure S17). The current density increase upon light illumination indicated that photocurrent was generated by $[Ru^{II}(bpy)_3]$-MoS_2.

To verify the role of surface tethered $[Ru^{II}(bpy)_3]^{2+}$ in the photocurrent generation, a control experiment was performed by monitoring the current responses of the ce-1T-MoS_2 and $[Ru^{II}(bpy)_3]$-MoS_2 cathodes at an applied bias potential of -0.33 V vs. RHE (the minimum potential required to drive HER using the ce-1T-MoS_2 electrode) with chopped light illumination in 60 s intervals (Figures 5). Both ce-1T-MoS_2 and $[Ru^{II}(bpy)_3]$-MoS_2 displayed steady and recyclable photo-enhanced current responses. The photosensitivity of the ce-1T-MoS_2 cathode can be ascribed to the existence of the semiconducting 2H-phase in ce-1T-MoS_2 sample.[31, 49] Nevertheless, a higher current density enhancement was achieved with a value of ΔJ = 33 μA/cm^2 for $[Ru^{II}(bpy)_3]$-MoS_2, compared to 10 μA/cm^2 for ce-1T-MoS_2, suggesting a higher photocurrent generation by $[Ru^{II}(bpy)_3]$-MoS_2. In addition, a steeper slope was observed along the downhill of photocurrent-time (*j*-t) curve for $[Ru^{II}(bpy)_3]$-MoS_2, reflecting a faster photocurrent generation rate.

Considering that the photocurrent onset potential depends on the photovoltage produced by illumination of light absorbers and the overpotential required for driving the HER process, two control experiments were performed to gain more insight on the PEC performance of $[Ru^{II}(bpy)_3]$-MoS_2 for HER. Firstly, the dark catalytic activity of the ce-1T-MoS_2 and $[Ru^{II}(bpy)_3]$-MoS_2 were measured (Figure S16). The $[Ru^{II}(bpy)_3]$-MoS_2 displayed a dark onset potential of -0.40 V vs. RHE when J = -0.2 mA/cm^2, whereas the ce-1T-MoS_2 showed a dark onset potential of -0.34 V vs. RHE (J = -200 μA/cm^2). The lower activity of $[Ru^{II}(bpy)_3]$-MoS_2 is not surprising because of the lower density of HER active sites and decreased intra-layer conductivity by surface functionalization treatment.[49-50] The photovoltage produced in ce-1T-MoS_2 and $[Ru^{II}(bpy)_3]$-MoS_2 was estimated by the difference between dark onset potential and photocurrent onset potential when J = -200 μA/cm^2. For $[Ru^{II}(bpy)_3]$-MoS_2, the photovoltage was calculated to be 50 mV, while ce-1T-MoS_2 only produced a photovoltage of 20 mV.

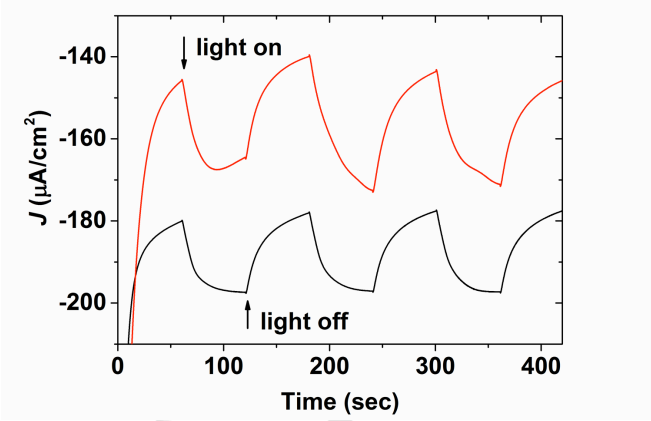

Figure 5. Chronoamperometry measurement at E = -0.33 V vs. RHE with ce-1T-MoS_2 (black) and $[Ru^{II}(bpy)_3]$-MoS_2 (red) deposited electrodes in 10 mM ascorbic acid aqueous solution (pH = 3) under chopped light irradiation.

To evaluate the role of the covalent linkage in $[Ru^{II}(bpy)_3]$-MoS_2, a control experiment was carried out by simply adding 2 molar equivalents of $[Ru^{II}(bpy)_2(5\text{-Me-bpy})](PF_6)_2$ to ce-1T-MoS_2 and performing a chronoamperometry measurement at E = -0.33 V vs. RHE. The photocurrent response of the non-tethered mixture against $[Ru^{II}(bpy)_3]$-MoS_2 (Figure S18) revealed that $[Ru^{II}(bpy)_3]$-MoS_2 demonstrated an enhanced photocurrent generation as well as a prompt light on/off switching response compared to the non-tethered mixture. This is most likely attributed to the presence of covalent linkages in $[Ru^{II}(bpy)_3]$-MoS_2, which inhibited the photo-generated electron-hole recombination and facilitated the efficient interfacial charge transfer, enabling the improved photocurrent generation.

In conclusion, covalent functionalization of chemically exfoliated MoS_2 nanosheets with a $[Ru^{II}(bpy)_3]^{2+}$ dye was accomplished. This was achieved by preparing bpy-functionalized MoS_2 and reacting it with $[Ru^{II}(bpy)_2Cl_2]$. The functionalized materials were characterized by DRIFT, electronic extinction, XPS, and Raman spectroscopies, and SEM. Three-electrode PEC measurement of $[Ru^{II}(bpy)_3]$-MoS_2 demonstrated a significant improvement of photocurrent generation compared to non-functionalized 1T-MoS_2. Given the ease of preparation of such complex-MoS_2 constructs, such synthetic strategies can be utilized in a modular fashion for the modification of MoS_2 and other 2D transition metal dichalcogenides toward customizable HER photocatalysts.

Acknowledgements

This publication has emanated from research supported by a research grant from Science Foundation Ireland (SFI/12/RC/2278). Research in the McDonald lab is supported in part by research grants from SFI (SFI/15/RS-URF/3307) and the European Union (ERC-2015-STG-678202).

Keywords: two-dimensional materials • transition metal dichalcogenides • covalent functionalization • dye-sensitized • photocatalytic HER

[1] M. G. Walter, E. L. Warren, J. R. McKone, S. W. Boettcher, Q. Mi, E. A. Santori, N. S. Lewis, *Chem. Rev.* **2010**, *110*, 6446-6473.
[2] Y. Wang, Q. Wang, X. Zhan, F. Wang, M. Safdar, J. He, *Nanoscale* **2013**, *5*, 8326-8339.
[3] C.-Y. Lee, H. S. Park, J. C. Fontecilla-Camps, E. Reisner, *Angew. Chem. Int. Ed.* **2016**, *55*, 5971-5974.
[4] T. Abbasi, S. A. Abbasi, *Renew. Sustain. Energy Rev.* **2011**, *15*, 3034-3040.
[5] A. J. Bard, M. A. Fox, *Acc. Chem. Res.* **1995**, *28*, 141-145.
[6] T. Hisatomi, J. Kubota, K. Domen, *Chem. Soc. Rev.* **2014**, *43*, 7520-7535.
[7] J. A. Turner, *Science* **2004**, *305*, 972-974.
[8] J. R. Rostrup-Nielsen, *Catal. Rev.* **2004**, *46*, 247-270.
[9] B. A. Pinaud, J. D. Benck, L. C. Seitz, A. J. Forman, Z. Chen, T. G. Deutsch, B. D. James, K. N. Baum, G. N. Baum, S. Ardo, H. Wang, E. Miller, T. F. Jaramillo, *Energy Environ. Sci.* **2013**, *6*, 1983-2002.
[10] C. Xiang, A. Z. Weber, S. Ardo, A. Berger, Y. Chen, R. Coridan, K. T. Fountaine, S. Haussener, S. Hu, R. Liu, N. S. Lewis, M. A. Modestino, M. M. Shaner, M. R. Singh, J. C. Stevens, K. Sun, K. Walczak, *Angew. Chem. Int. Ed.* **2016**, *55*, 12974-12988.
[11] A. Kudo, Y. Miseki, *Chem. Soc. Rev.* **2009**, *38*, 253-278.

[12] M. Chhowalla, H. S. Shin, G. Eda, L. J. Li, K. P. Loh, H. Zhang, *Nat. Chem.* **2013**, *5*, 263-275.

[13] X. Huang, Z. Zeng, H. Zhang, *Chem. Soc. Rev.* **2013**, *42*, 1934-1946.

[14] D. Voiry, A. Goswami, R. Kappera, e. SilvaCecilia de Carvalho Castro, D. Kaplan, T. Fujita, M. Chen, T. Asefa, M. Chhowalla, *Nat. Chem.* **2015**, *7*, 45-49.

[15] H. Tributsch, J. C. Bennett, *J. Electroanal. Chem. Interfacial. Electrochem.* **1977**, *81*, 97-111.

[16] Y. Yan, B. Xia, Z. Xu, X. Wang, *ACS Catal.* **2014**, *4*, 1693-1705.

[17] T. F. Jaramillo, K. P. Jørgensen, J. Bonde, J. H. Nielsen, S. Horch, I. Chorkendorff, *Science* **2007**, *317*, 100-102.

[18] D. Voiry, M. Salehi, R. Silva, T. Fujita, M. Chen, T. Asefa, V. B. Shenoy, G. Eda, M. Chhowalla, *Nano Lett.* **2013**, *13*, 6222-6227.

[19] H. Wang, Z. Lu, S. Xu, D. Kong, J. J. Cha, G. Zheng, P.-C. Hsu, K. Yan, D. Bradshaw, F. B. Prinz, Y. Cui, *Proc. Natl. Acad. Sci. U. S. A.* **2013**, *110*, 19701-19706.

[20] J. D. Benck, T. R. Hellstern, J. Kibsgaard, P. Chakthranont, T. F. Jaramillo, *ACS Catal.* **2014**, *4*, 3957-3971.

[21] F. Wang, T. A. Shifa, X. Zhan, Y. Huang, K. Liu, Z. Cheng, C. Jiang, J. He, *Nanoscale* **2015**, *7*, 19764-19788.

[22] L. F. Schneemeyer, M. S. Wrighton, *J. Am. Chem. Soc.* **1979**, *101*, 6496-6500.

[23] H. Shi, R. Yan, S. Bertolazzi, J. Brivio, B. Gao, A. Kis, D. Jena, H. G. Xing, L. Huang, *ACS Nano* **2013**, *7*, 1072-1080.

[24] Q. Ding, F. Meng, C. R. English, M. Cabán-Acevedo, M. J. Shearer, D. Liang, A. S. Daniel, R. J. Hamers, S. Jin, *J. Am. Chem. Soc.* **2014**, *136*, 8504-8507.

[25] B. Seger, A. B. Laursen, P. C. K. Vesborg, T. Pedersen, O. Hansen, S. Dahl, I. Chorkendorff, *Angew. Chem. Int. Ed.* **2012**, *51*, 9128-9131.

[26] Y. Hou, B. L. Abrams, P. C. K. Vesborg, M. E. Björketun, K. Herbst, L. Bech, A. M. Setti, C. D. Damsgaard, T. Pedersen, O. Hansen, J. Rossmeisl, S. Dahl, J. K. Nørskov, I. Chorkendorff, *Nat. Mater.* **2011**, *10*, 434-438.

[27] R. J. Britto, J. D. Benck, J. L. Young, C. Hahn, T. G. Deutsch, T. F. Jaramillo, *J. Phys. Chem. Lett.* **2016**, *7*, 2044-2049.

[28] X. Zong, Y. Na, F. Wen, G. Ma, J. Yang, D. Wang, Y. Ma, M. Wang, L. Sun, C. Li, *Chem. Commun.* **2009**, 4536-4538.

[29] Y.-J. Yuan, Z.-T. Yu, X.-J. Liu, J.-G. Cai, Z.-J. Guan, Z.-G. Zou, *Sci. Rep.* **2014**, *4*, 4045.

[30] Y.-J. Yuan, Z.-T. Yu, Y.-H. Li, H.-W. Lu, X. Chen, W.-G. Tu, Z.-G. Ji, Z.-G. Zou, *Appl. Catal. B: Environ.* **2016**, *181*, 16-23.

[31] U. Maitra, U. Gupta, M. De, R. Datta, A. Govindaraj, C. N. R. Rao, *Angew. Chem. Int. Ed.* **2013**, *52*, 13057-13061.

[32] Y.-J. Yuan, D. Chen, J. Zhong, L.-X. Yang, J. Wang, M.-J. Liu, W.-G. Tu, Z.-T. Yu, Z.-G. Zou, *J. Mater. Chem. A* **2017,** *5*, 15771-15779.

[33] Y.-J. Yuan, D. Chen, S. Yang, L.-X. Yang, J.-J. Wang, D. Cao, W. Tu, Z.-T. Yu, Z.-G. Zou, *J. Mater. Chem. A* **2017,** *5*, 21205-21213.

[34] Y.-J. Yuan, Z.-J. Ye, H.-W. Lu, B. Hu, Y.-H. Li, D.-Q. Chen, J.-S. Zhong, Z.-T. Yu, Z.-G. Zou, *ACS Catal.* **2016,** *6*, 532-541.

[35] C. Backes, N. C. Berner, X. Chen, P. Lafargue, P. LaPlace, M. Freeley, G. S. Duesberg, J. N. Coleman, A. R. McDonald, *Angew. Chem. Int. Ed.* **2015**, *54*, 2638-2642.

[36] X. Chen, N. C. Berner, C. Backes, G. S. Duesberg, A. R. McDonald, *Angew. Chem. Int. Ed.* **2016**, *55*, 5803-5808.

[37] X. Chen, A. R. McDonald, *Adv. Mater.* **2016**, *28*, 5738-5746.

[38] K. C. Knirsch, N. C. Berner, H. C. Nerl, C. S. Cucinotta, Z. Gholamvand, N. McEvoy, Z. Wang, I. Abramovic, P. Vecera, M. Halik, S. Sanvito, G. S. Duesberg, V. Nicolosi, F. Hauke, A. Hirsch, J. N. Coleman, C. Backes, *ACS Nano* **2015**, *9*, 6018-6030.

[39] M. Grätzel, *Acc. Chem. Res.* **2009**, *42*, 1788-1798.

[40] G. Eda, H. Yamaguchi, D. Voiry, T. Fujita, M. Chen, M. Chhowalla, *Nano Lett.* **2011**, *11*, 5111-5116.

[41] K. R. Bargawi, A. Llobet, T. J. Meyer, *Journal of the American Chemical Society* **1988**, *110*, 7751-7759.

[42] C. E. McCusker, J. K. McCusker, *Inorg. Chem.* **2011**, *50*, 1656-1669.

[43] A. M. Beiler, D. Khusnutdinova, S. I. Jacob, G. F. Moore, *Ind. Eng. Chem. Res.* **2016**, *55*, 5306-5314.

[44] However, the presence of non-coordinated pyridyl-N species suggested that not all the surface tethered bipyridine moieties were bonded to Ru(II) center forming complex, thus the $[Ru^{II}(bpy)_3]$-MoS_2 actually contained both non-coordinated bipyridine moieties and [RuII(bpy)3]2+-complexes.

[45] D. Marton, K. J. Boyd, A. H. Al-Bayati, S. S. Todorov, J. W. Rabalais, *Phys. Rev. Lett.* **1994**, *73*, 118-121.

[46] C. Backes, R. J. Smith, N. McEvoy, N. C. Berner, D. McCloskey, H. C. Nerl, A. O'Neill, P. J. King, T. Higgins, D. Hanlon, N. Scheuschner, J. Maultzsch, L. Houben, G. S. Duesberg, J. F. Donegan, V. Nicolosi, J. N. Coleman, *Nat. Commun.* **2014**, *5*, 4576.

[47] X. Zhang, X.-F. Qiao, W. Shi, J.-B. Wu, D.-S. Jiang, P.-H. Tan, *Chem. Soc. Rev.* **2015**, *44*, 2757-2785.

[48] S. Jiménez Sandoval, D. Yang, R. F. Frindt, J. C. Irwin, *Phys. Rev. B* **1991**, *44*, 3955-3962.

[49] R. Peng, L. Liang, Z. D. Hood, A. Boulesbaa, A. Puretzky, A. V. Ievlev, J. Come, O. S. Ovchinnikova, H. Wang, C. Ma, M. Chi, B. G. Sumpter, Z. Wu, *ACS Catal.* **2016**, *6*, 6723-6729.

[50] D. A. Henckel, O. Lenz, B. M. Cossairt, *ACS Catal.* **2017**, *7*, 2815-2820.

Table of Contents

COMMUNICATION

Covalent tethering of 1T-MoS_2 nanosheets with $[Ru^{II}(bpy)_3]^{2+}$ photosensitizers yields photosensitising H_2-evolution catalysts. The $[Ru^{II}(bpy)_3]$-MoS_2 hybrid exhibited a significantly enhanced photocurrent and H_2-evolution performance.

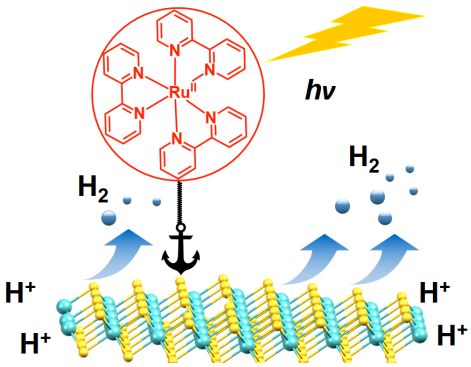

*Xin Chen, David McAteer, Cormac McGuinness, Ian Godwin, Jonathan N. Coleman, Aidan R. McDonald**

Page No. – Page No.

Ru^{II} photosensitizer functionalized two-dimensional MoS_2 for light-driven hydrogen evolution